

Article

Short-Wavelength Infrared Characteristics and Indications of Exploration of the Jiawula Silver–Lead–Zinc Deposit in Inner Mongolia

Lei Wang, Zian Yang *, Weixuan Fang, Dewen Wu, Zhiqiang Liu and Gao Guan

China Non-Ferrous Metals Resource Geological Survey, No.5 Courtyard Area 4, Anwai Beiyuan, Chaoyang District, Beijing 100012, China; wla2009@sina.cn (L.W.); weixuanfang@163.com (W.F.); wdewen@163.com (D.W.); qiang198307142024@163.com (Z.L.); guangao_xl@sina.com (G.G.)

* Correspondence: yzaldy88@126.com; Tel./Fax: +86-10-84925807

Abstract: For the Jiawula lead–zinc deposit, as easily accessible resources become depleted, mines are becoming deeper to replenish ore reserves. Identifying large, continuous, and high-grade ore bodies in deep areas has become a daunting problem. Moreover, separating lead–zinc-bearing complex ore bodies from waste material and extracting them from associated minerals are also difficult. Thus, pioneering exploratory strategies and technological methodologies are required to make breakthroughs in mineral discovery. Based on extensive-scale structural lithofacies mapping, this paper uses short-wave infrared (SWIR) spectroscopy technology to investigate hydrothermal alteration minerals in the mining area. It has identified a total of 16 hydroxyl-bearing alteration minerals, including chlorite, muscovite, illite, calcite, ankerite, kaolinite, and smectite. These minerals establish zoning characteristics around the ore bodies and on their flanks. They comprise a segmented assemblage that follows the pattern of comb-textured quartz–illite–chlorite–carbonate → muscovite–illite–chlorite–ankerite → illite–smectite–chlorite → chlorite–kaolinite–calcite. Deep-zone illitization with a lower Al–OH absorbance peak wavelength (<2206 nm) and higher crystallinity indices (>1.1) and chloritization with higher Fe–OH absorbance peak wavelengths (>2254) and higher crystallinity indices (>3.0) are indicators of potential hydrothermal centers in the deeper regions. By finding hydrothermal centers and connecting their spatial distribution with existing ore bodies, a pertinent relationship between diabase + andesite, Fe-chlorite + illite, and high-grade mineralization has been established. They correspond well with the lithology-alteration mineralization. This research provides a basis for predicting the positioning of concealed ore bodies deep inside a mine or at the periphery.

Keywords: tectonic lithofacies; shortwave infrared; hydrothermal alteration; alteration zone; hydrothermal center; Jiawula



Citation: Wang, L.; Yang, Z.; Fang, W.; Wu, D.; Liu, Z.; Guan, G. Short-Wavelength Infrared Characteristics and Indications of Exploration of the Jiawula Silver–Lead–Zinc Deposit in Inner Mongolia. *Appl. Sci.* **2024**, *14*, 3658. <https://doi.org/10.3390/app14093658>

Academic Editor: Nikolaos Koukoulas

Received: 4 February 2024

Revised: 22 April 2024

Accepted: 23 April 2024

Published: 25 April 2024



Copyright: © 2024 by the authors. Licensee MDPI, Basel, Switzerland. This article is an open access article distributed under the terms and conditions of the Creative Commons Attribution (CC BY) license (<https://creativecommons.org/licenses/by/4.0/>).

1. Introduction

The mapping of mineral alteration primarily relies on hyperspectral measurement techniques, but the shortwave infrared (SWIR) band is the most sophisticated and popular technique [1–3]. The commonly used technologies for high-resolution SWIR and near-infrared mineral measurements include the Portable Infrared Mineral Analyzer (PIMA) from Australia, the TerraSpec® Halo handheld analyzer developed by ASD in the United States, and the PNIRS system produced by the Nanjing Institute of Geology and Mineral Resources in China [4–11]. In recent years, SWIR spectroscopy has been successfully applied in the exploration and prospecting of porphyry, shallow low-temperature hydrothermal, and skarn-type deposits [4–7,12–21], and remarkable results have been achieved in the discovery of concealed ore bodies as well as the deep and peripheral mining areas [12–21]. SWIR spectroscopy is characterized by no need for sample preparation, short testing time, convenience, and speed. Compared to traditional mineral identification methods, it can

effectively save on sample preparation and testing time, while also better controlling the cost of testing work [1–15]. Previous studies of SWIR's application have covered areas such as Rodalquilar in Andalusia, Spain; Hauraki in New Zealand; Cananea in Mexico; Mongolia; Thailand; Hawaii in America; Zijin Mountain in Fujian Province; Nuri, Demingding, Tiegelongnan, and Niancun in Xizang Autonomous Region; Tonglushan in Southeast Hubei Province; East Tianshan in Xinjiang Uygur Autonomous Region; and Wunugetushan and Ganzhuershande in Inner Mongolia Autonomous Region, and significant results have been achieved. Van der Meer et al. show the case of the Rodalquilar epithermal system of the southern Spanish Gabo de Gata volcanic area using HyMAP airborne hyperspectral images [3]. Simpson, M.P., shows most illite has a crystallinity value of >1.1 and illite–smectite < 1.1 as calculated from reflectance spectra, and a general increase in crystallinity value with depth [4]. Thompson, J.B., shows the application of reflectance spectroscopy at the Cananea Cu–porphyry deposit, Mexico [5]. Dill, H.G., shows PIMA is the only method for obtaining first-hand information on the mineral composition in the field [6]. Calvin, W.M., et al. successfully identified a wide variety of phyllosilicates, zeolites, opal, calcite, iron oxides, and hydroxides and noted depth-associated changes in alteration minerals, patterns, or zones [7]. Xu Chao et al. used the crystallinity index of illite (ISM) and the absorption peak position of illite at 2200 nm as indicators for the discovery of a copper–molybdenum mineralization section in Zijin Mountain [14]. The Gangdise metallogenic belt in Tibet includes several porphyry and shallow low-temperature hydrothermal deposits, such as Qulong, Jiama, Nuri, Demingding, Tiegelongnan, Niancun, and Sinong. The studies have involved minerals such as muscovite, illite, alunite, kaolinite, and chlorite. By extracting features from the spectral curves and analyzing the spatial variation patterns, the hydrothermal mineralization centers can be determined [15–20]. Zhang Shitao et al. proposed that the high Fe–OH characteristic absorption peak value of chlorite (Pos2250 > 2253 nm) indicated the mineralization center of the skarn-type deposit in Tonglushan [15]. Chen Shoubo et al. concluded that the sericite alteration zone near the greenstone belt with an absorption peak of chlorite Fe–OH > 2253 nm can serve as an indicator for the exploration in the Yuhai copper ore district of East Tianshan, Xinjiang [18]. Liu Xinxing et al. analyzed the SWIR and thermal infrared spectra of borehole core samples to study the alteration and crystallinity of illite–sericite from the Wunugetushan and Ganzhuershande porphyry–hydrothermal deposits in Inner Mongolia [21,22]. The crystallinity index of illite (ISM) is proportional to the degree of mineralization, and a high ISM value indicates the hydrothermal center. These studies show that SWIR mineral measurement techniques are effective in mineral alteration mapping in the geological exploration of mining areas.

The four large-scale deposits, namely the Jiawula silver–lead–zinc deposit, Chaganbulagen silver–lead–zinc deposit, Wunugetushan copper–molybdenum deposit, and Erentaolegai silver deposit, which were discovered from the 1970s to 1990s in the Manzhouli and New Barag Right Banner of Inner Mongolia, are important non-ferrous metal resource bases in the Manzhouli region of Inner Mongolia, China [23–28]. Although they are still undergoing mining, the extraction depths are increasing and challenged by resource depletion, especially for the Jiawula silver–lead–zinc deposit. The Jiawula mine urgently needs to make new breakthroughs so that it can obtain sufficient resource reserves for sustainable development and future production. It actively seeks solutions by looking for new ore bodies in the deeper parts of the main ore body and its northwest. It has adopted advanced mining technology to upgrade the facilities and pushed forward exploration projects to address resource depletion. The deposit is primarily composed of subvolcanic diorite. The alteration types, zonation, morphology, and scale can best reflect the mineralization and formation of the mine [29–39]. This provides a good testing ground for mineral alteration mapping.

Based on the large-scale litho-tectonic mapping, this study used the TerraSpec® Halo portable SWIR analyzer to conduct mineral alteration mapping. The test was performed in the underground tunnels and drill cores from the deep and peripheral areas of the Jiawula mining district of Inner Mongolia. Information about hydroxyl-bearing silicate minerals,

particularly the spectra of chemical bonds such as Al–OH, Fe–OH, Mg–OH, and CO_3^{2-} , was obtained. Parameters of the hydrothermal alteration system, mineral abundance, distribution, and crystallinity were extracted as markers for mineral exploration. By delineating zones of mineral alterations and hydrothermal centers, the study provides technical support for the exploration of the Jiawula deposit in deep and peripheral areas.

2. Mineralization Geological Background

2.1. Regional Geology

The study area is located on the western side of the Eerguna–Hulun deep fault zone (see Figure 1), along the northern northwest-trending structural zone of the Jiawula–Adunchulu volcanic rift in the Manzhouli–Xin Barag Right Banner volcanic uplift [24–26]. The exposed strata and rocks consist of various formations, including the Middle Jurassic Wanbao Formation, which is composed of andesite, rhyolite, sandstone, mudstone, and carbonaceous shale. It is overlain by the Middle Jurassic Tamulangou Formation, which comprises intermediate basic volcanics and volcanic breccias, as well as the Upper Jurassic Mamantugou Formation, composed of volcanic tuffs and intrusive intermediate to acidic subvolcanic rocks. Within this region, there are important deposits such as the Jiawula silver–lead–zinc deposit, Chaganbulagen silver–lead–zinc deposit, Wunugetushan copper–molybdenum deposit, and Erentaolegai silver deposit (see Figure 1).

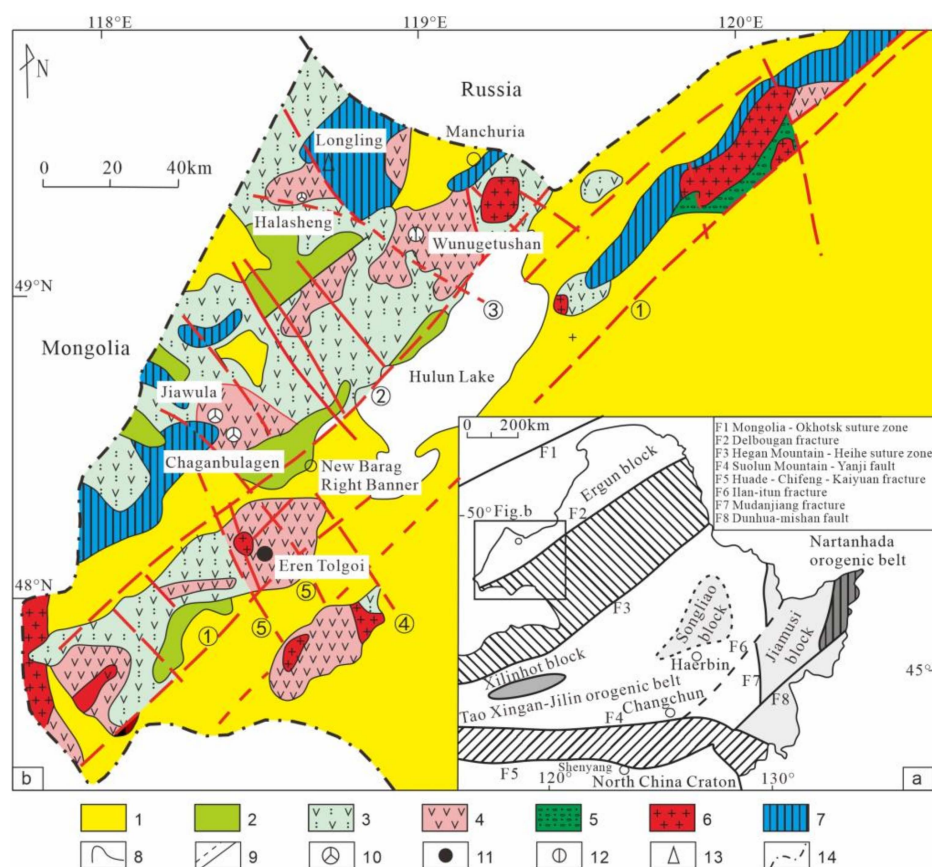


Figure 1. Regional tectonic geological map of the study area (Adapted with permission from Ref. [31]). 1. Tertiary and Quaternary strata; 2. Lower Cretaceous sandstone and mudstone; 3. Upper Jurassic–Lower Cretaceous acidic to intermediate volcanic rocks; 4. Middle Jurassic basic to intermediate volcanic rocks; 5. Middle Jurassic sandstone and conglomerate; 6. Yanshanian granites; 7. Middle Jurassic geological formation; 8. geological boundary; 9. observed or inferred faults; 10. silver–lead–zinc deposit; 11. silver deposit; 12. copper–molybdenum deposit; 13. copper–zinc–tin deposit; 14. national border; ① Deerbugan Fault; ② Eerguna River–Hulun Fault; ③ Hanigou Fault; ④ Muhaer Fault; ⑤ Jiawula–Chaganbulagen Fault.

2.2. Mining Geology

In the mining area, the exposed strata consist of Middle Jurassic volcanic rocks, continental sedimentary rocks, and Upper Jurassic volcanic rocks. Based on time sequence, the formations range from the Middle Jurassic Wanbao Formation (J_2wb) to the Tamulangou Formation (J_2tm) to the Upper Jurassic Mamantugou Formation (J_3mn). The mineral deposits were likely formed by subsequent intrusion of portions of magma, and they were controlled by activation of the tectonic structures during the late Yanshan period. The ore bodies comprise predominantly northwest- and north-northwest trending brittle-ductile structures and subvolcanic rocks on the edge (see Figure 2a,b). Among these structures, F1 controls the No. 1 ore body, F2 controls the No. 2 ore body, F3 controls the No. 2–44 ore body, F4 controls the No. 12 ore body, and F5 controls the No. 3 ore body. The Jurassic granite intrusions from the Hercynian period are widespread northeast of the No. 1 ore body. The Yanshan period subvolcanic rocks exhibit multiple intrusive phases. The dominant rock type in the early stages is diorite. In later stages, quartz–feldspar porphyry, quartz porphyry, quartzite, and quartz–monzonite porphyry become dominant (see Figure 2a).

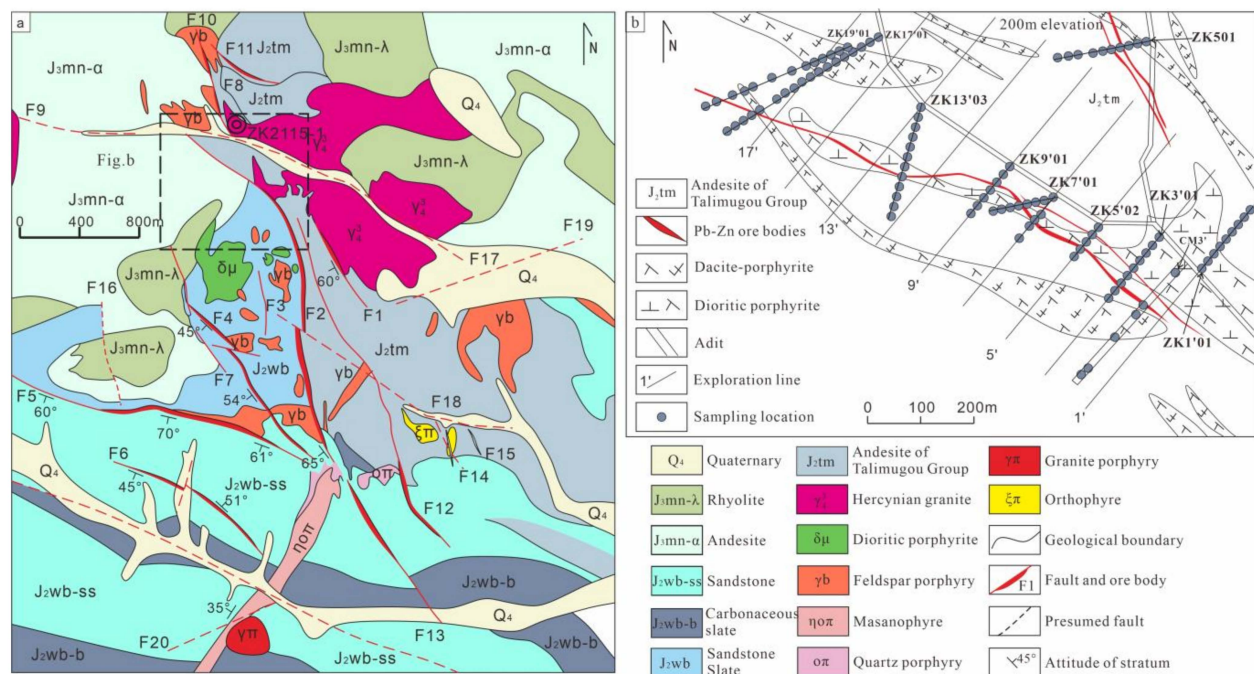


Figure 2. Geological and mineralization map of Jiawula (a) and sampling locations (b).

3. Sample Collection and Data Processing

3.1. Sample Collection and Testing

The mining area was surveyed using the TerraSpec[®] Halo portable mineral analyzer from the American company ASD. Samples were taken mostly from drill holes and tunnels in the No. 2 ore body of the Jiawula deposit. Tunnel samples were obtained from the midpoints at 0 m and 200 m, while drill hole samples were from drill hole ZK2115-1 and from the midpoints of two tunnels (see Figure 2). Based on lithology, alteration assemblages, and intensity, samples were prepared in the tunnel with a sample spacing of 8–10 m, except for areas of intense alteration over which a 2–3 m spacing was used, and for areas of strong mineralization, the spacing was further narrowed to 1–2 m. As for the drill hole sampling, the spacing was typically 3 m, and it was reduced to 1–2 m in strongly altered sections and to 0.3–0.5 m in the presence of mineralized bodies. For surrounding rocks above and below the mineralized bodies, the sample spacing was changed to 0.5–1 m. Detailed and on-site maps of structure and lithology were referred to for the sampling, which mainly focused on veins (particularly carbonate, calcite, and quartz veins), sheet-like alterations

(like chloritization, illitization), mineralized bodies, and the surrounding rocks above and below the ore (see Figure 3).

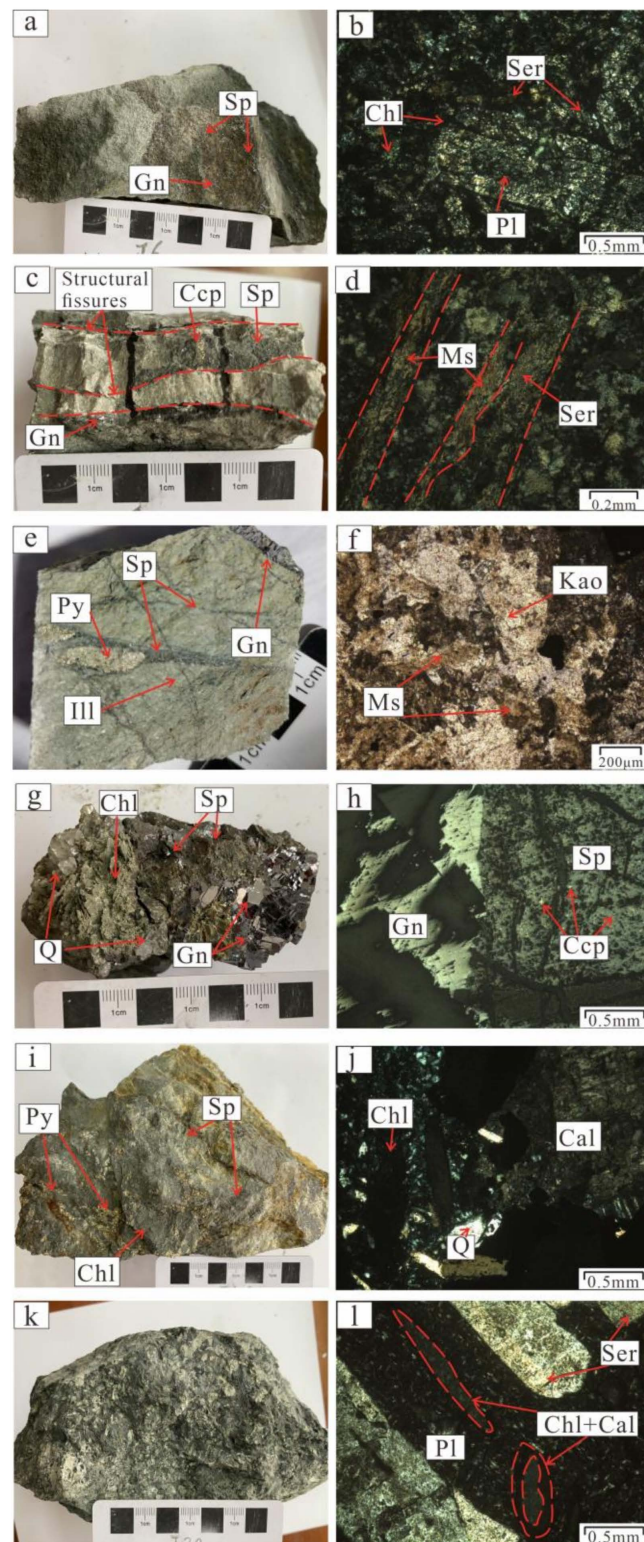


Figure 3. Photographs of the main rock and mineral alterations in the Jiawula deposit. (a) The altered plagioclase gneiss containing disseminated sphalerite shows a star-like distribution pattern, often associated with galena. (b) The matrix commonly displays sericitization and chloritization, while pyroxene is altered to chlorite. (c) Sphalerite mineralization occurs within quartz porphyry, filling vein-like structures along fractures, with an enclosed solid solution of chalcopyrite. (d) Silicification

of quartz, white mica, and sericite fills fractures in a vein-like pattern, with sericite occurring as microscopic flakes. Some consist of iron staining. (e) The intense illitization of biotite gneiss yields a yellow-green hue, with later sphalerite-galena network veins and fine-grained clusters of pyrite observed at the edges. (f) Feldspar cores and calcium-rich areas are altered to kaolinite and illite (water-white mica). (g) Quartz veins are filled with hydrothermal breccia, with blocky galena and cemented sphalerite, and show chloritization on the surface. (h) Galena forms granular aggregates, while sphalerite occurs in clustered distributions, often enclosing a fine-grained solid solution of pyrite. (i) Sphalerite-illitization alteration occurs in green-chloritized andesite. (j) Chlorite occurs as aggregated microscopic flakes, while silicified quartz appears in columnar form, and calcite forms vein-like distributions within rock structural fractures. (k) The surface of the andesite displays chloritization. (l) Plagioclase phenocrysts are extensively altered by various levels of sericitization and kaolinization, while pyroxene is replaced by calcite and chlorite. The rock contains almond-shaped inclusions that are filled with chlorite and calcite. Q—quartz; Py—pyrite; Gn—galena; Sp—sphalerite; Ccp—chalcocopyrite; Chl—chlorite; Ill—illite; Ser—sericite; Pl—plagioclase; Ms—muscovite; Cal—calcite; Kao—kaolinite.

Tunnel samples were tested indoors. Prior to testing, the samples were carefully cleaned and dried. Drill hole samples were tested in situ after the cores were washed and air-dried outdoors. The researcher would test 1 to 3 points of each sample, and the scan of each point lasted 15 to 20 s. During the testing, we ensured that the test results corresponded to related geological information and location and saved the testing data promptly in a computer for analysis.

3.2. Data Processing

Spectral Geologist (TSG 8.0) spectral interpretation software was adopted for data processing in this study. The tested spectra were matched with those in the spectral database to identify mineral types and relative abundances. The Aux matching function of Spectral Geologist extracts characteristic spectral bands' parameters, such as the wavelength, absorption depth, full width at half maximum (FWHM), and integrated intensity. For instance, the muscovite mineral group (muscovite and illite) was interpreted within the spectral range of 2195–2200 nm (Al–OH absorption peak). The interpretation range for chlorite minerals (Fe–Mg chlorite, Mg–chlorite, and Fe–chlorite) was 2245–2265 nm (Fe–OH absorption peak). Based on field recordings and spectral absorption depths, we manually interpreted the altered minerals that had been interpreted by TSG. After selecting the minerals according to lithological sections, we finally identified the species of the altered minerals.

4. Test Results and Interpretation

4.1. Types of Altered Minerals

The samples collected from the Jiawula lead–zinc–silver deposit contained a total of 16 types of altered minerals (Figure 4). The types of minerals include Fe–Mg chlorite, Mg–chlorite Fe–chlorite, muscovite, paragonite, phengite, muscovite illite, paragonite illite, phengite illite, calcite, ankerite, kaolinite, and smectite. The highly crystalline white micas can be referred to by their mineral name muscovite, phengite, or paragonite. The illitic white micas also display compositional substitution and can be referred to as illite, phengitic illite, or paragonitic illite. In general, the mineral species of muscovite group, illite group, and chlorite group could not be accurately determined by rock specimens and microscopic identification. Examples include muscovite (muscovite, paragonite, and phengite), illite (muscovite illite, paragonite illite, and phengite illite), and chlorite (Fe–Mg chlorite, Mg–chlorite, and Fe–chlorite). Therefore, in this study, the muscovite group, illite group, and chlorite group minerals are not specifically distinguished when the altered mineral assemblages of the tunnel and borehole are zoned. Based on the identification by the TerraSpec mineral spectrometer and field-based manual alteration recognition, this study categorized muscovite, phengite, and paragonite as muscovite minerals and muscovite

illite, phengite illite, and paragonite illite as illite. Furthermore, it grouped Fe-Mg chlorite, Mg-chlorite, and Fe-chlorite in the category of chlorite minerals.

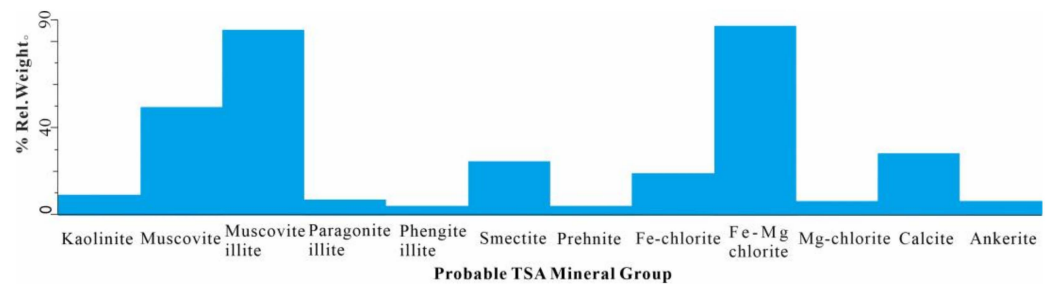


Figure 4. Frequency distribution of altered minerals in the Jiawula deposit.

TSG was adopted to identify and interpret the types and mass fractions of altered minerals. During the identification and categorization of altered minerals, we only included minerals with mass fractions greater than 0.2 and ignored those with fractions lower than 0.2 to enhance the accuracy. The TerraSpec mineral spectrometer could not identify quartz silicified veins, so they were often recognized as “NULL” or “Aspectral”. Therefore, the recognition and delineation of silicified zones were performed manually. Typical assemblages of altered minerals comprise muscovite–illite, muscovite–illite–chlorite, or illite–chlorite–calcite ± ankerite, while the silicified zones comprise illite–smectite–chlorite and muscovite–kaolinite.

4.2. Major SWIR Spectral Characteristics of Altered Minerals

(1) SWIR spectral characteristics of muscovite (illite) type

Muscovite minerals have two functional groups: OH + H₂O and Al–OH. High-crystallinity muscovite can be classified into common muscovite, phengite, and sodium muscovite. After the illitization of muscovite, the composition of the muscovite will change to illite, phengite illite, and sodium muscovite illite. The primary differences are as follows: common muscovite has a sharp absorption peak at a wavelength of 2190 nm; phengite has a sharp absorption peak at the wavelength between 2214 and 2225 nm; and sodium muscovite has a sharp absorption peak at the wavelength between 2184 and 2190 nm. The spectral curves of muscovite and illite are consistent. Their absorption peak wavelength for crystalline water (Pos1400) was near 1400 nm. For the adsorbed water wavelength (Pos1900), it was near 1900 nm, and for the Al–OH wavelength (Pos2200), the peak was near 2200 nm (Figure 5). The depth of their absorption peak represents the maximum depth near the absorption peak in the standardized reflectivity spectrum (Dep1400, Dep1900, Dep2200). Given the prominent absorption peak of Pos1900 in muscovite found in the Jiawula lead–zinc mine, 1900 nm was chosen as the center of adsorbed water, with an extraction radius of 15. The absorption peak of Pos2200 in muscovite was relatively sharp but drifting towards longer wavelengths. Therefore, 2205 nm was chosen as the center for Al–OH, with an extraction radius of 15. The crystallinity of muscovites (ISM) is expressed as the ratio of Al–OH absorption depth (Dep2200) to the absorption feature depth of adsorbed water at 1900 nm (Dep1900). Now that we had extracted the characteristic absorption peaks, absorption depths, and crystallinity from the samples, we used scatter plots to analyze the parameters in a systematic and statistical way and determined that the variation range of muscovite (illite)-type Pos2200 in this mining area was between 2200.26 and 2212.72 nm, with an average value of 2206.49, and the range of ISM values was 0.058–3.193, with an average value of 0.96.

(2) SWIR spectral characteristics of chlorite type

The three primary types of chlorite minerals are Fe-Mg chlorite, Mg-chlorite and Fe-chlorite, and their main features are as follows: Mg-chlorite’s absorption peak for adsorbed water is at the 1394 nm wavelength, its peak for crystalline water is between 1880 and 1980 nm (Pos1900), and its absorption peak for Fe–OH is 2245 nm (Pos2250). The Mg–OH

absorption peak occurs at a 2325 nm wavelength (Pos2350), and a deeper absorption peak indicates more Mg-chlorite. Fe-Mg chlorite has an absorption peak of 1409 nm wavelength for adsorbed water, its wavelength for crystalline water is 2000 nm, its wavelength for Fe–OH is 2254 nm, and its wavelength for Mg–OH is 2347 nm. These wavelengths reflect typical features of Fe-Mg chlorite. Fe-chlorite's absorption peaks for crystalline water are between 1900 and 2000 nm; its absorption peak for Fe–OH is at 2261 nm (slightly shallower than the Mg–OH absorption peak), and the absorption peaks for Mg–OH are between 2355 and 2365 nm. A deeper absorption peak indicates more abundant Fe-chlorite in this area (Figure 5). Because of the steep absorption peak of Pos1900 in chlorite in the Jiawula lead–zinc mining area, 1900 nm was chosen as the center for adsorbed water, with an extraction radius of 15. Given the sharp absorption peak of Pos2250, 2250 nm became the center for Fe–OH, with a radius of 15. Due to the sharp absorption peak of Pos2350, 2350 nm was selected as the center for Mg–OH, with an extraction radius of 15. After measuring the characteristic absorption peaks, absorption depths, and crystallinity of the extracted samples, we created scatter plots to perform systematic and statistical analysis on the parameters and determined the variation range of chlorite-type Pos2250 in this mining area to be 2247.87–2260.05 nm, with an average value of 2253.96. The range of CSM values was 0.212–9.082, with an average value of 2.37.

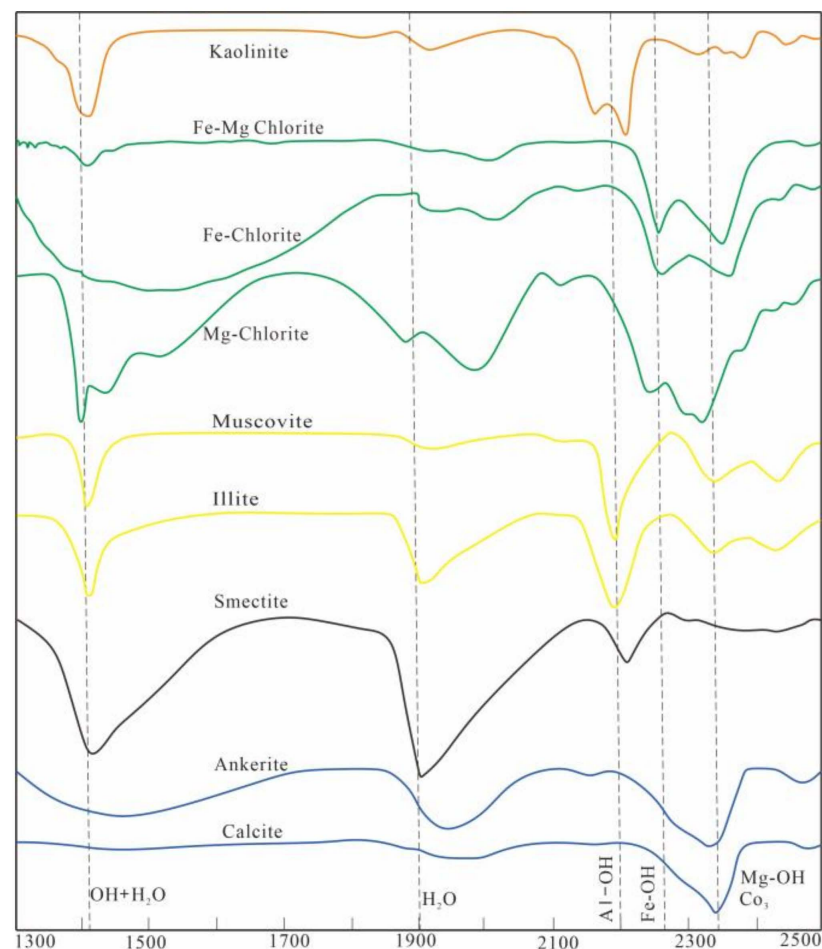


Figure 5. Absorption characteristics of standard minerals.

4.3. Alteration Mineral Assemblages and Alteration Zones

Based on the large-scale lithofacies mapping and alteration mineral mapping, this study adopted TSG spectral geological analysis software (version 8.0) to identify alteration of the core and tunnel samples extracted from the northern mining area. It selected ZK13'03 to investigate the middle section of the horizontal alteration zone at 200 m depth,

ZK20(0)1'02 to look into the middle section of the horizontal alteration zone at 0 m, and ZK2115-1 to examine the vertical alteration zone. Based on the alteration mineral assemblages, the analysis can be shown as follows:

(1) Borehole ZK19 (200) 13'03 can be divided into four alteration zones (Figure 6): (1) muscovite + illite + chlorite + calcite + smectite + ankerite, (2) muscovite + chlorite + calcite + smectite, (3) muscovite + illite + chlorite + kaolinite, and (4) chlorite + calcite + smectite + ankerite. Mg-chlorite was mainly distributed at the upper part of the borehole, while Fe-chlorite was mainly concentrated in the lower part.

(2) Borehole ZK20(0)1'02 can be divided into three alteration zones (Figure 7): (1) chlorite + calcite + ankerite + kaolinite, (2) muscovite + illite + chlorite + calcite, and (3) chlorite + ankerite. No Mg-chlorite was found in this borehole, and Fe-chlorite was mainly distributed in the lower part. Sericite illite was surrounded by ankerite on both sides.

(3) Borehole ZK2115-1 can be divided into five alteration zones: (1) illite + chlorite + calcite + smectite + kaolinite, (2) muscovite + illite + chlorite + calcite + smectite + ankerite, (3) muscovite + illite + chlorite + calcite + smectite, (4) chlorite + calcite + smectite, and (5) muscovite + illite + chlorite + calcite + smectite. Based on the content and frequency, we found that core samples were infilled by illite, Fe-Mg chlorite, calcite, and smectite (Figure 8). Mg-chlorite alteration occurred mainly in the upper part of the borehole, and Fe-chlorite was concentrated in the three blocks in the upper part of the borehole.

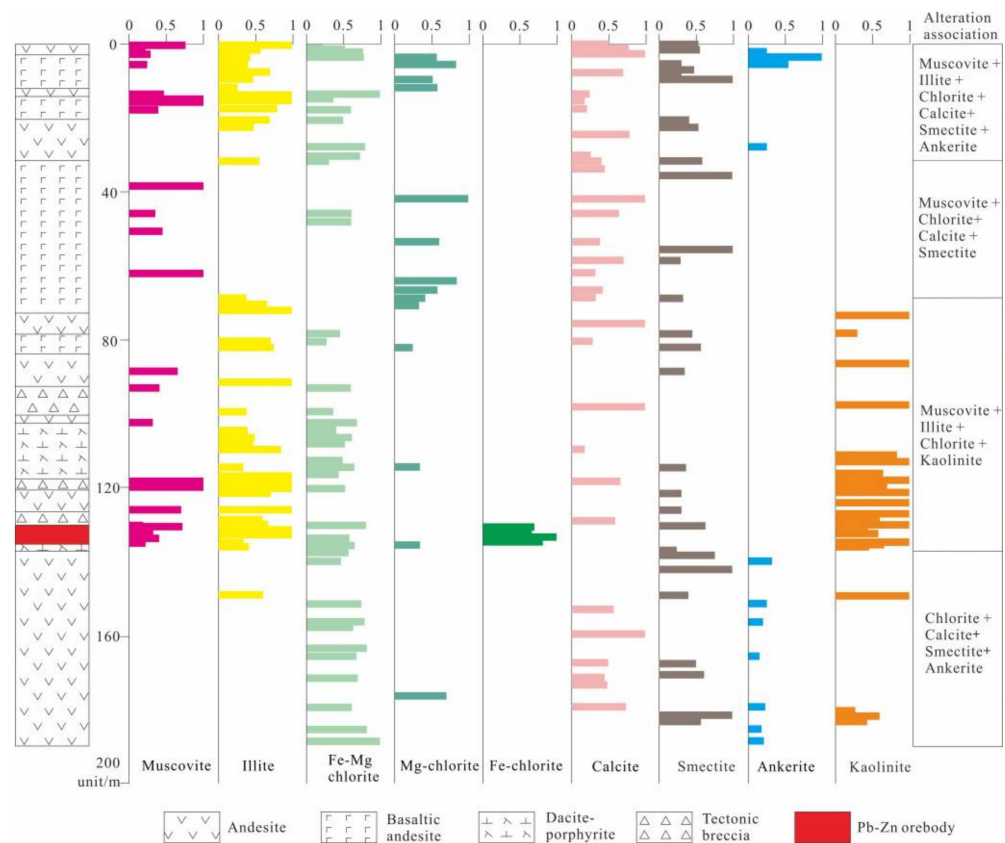


Figure 6. Alteration mineral zones in ZK13'03.

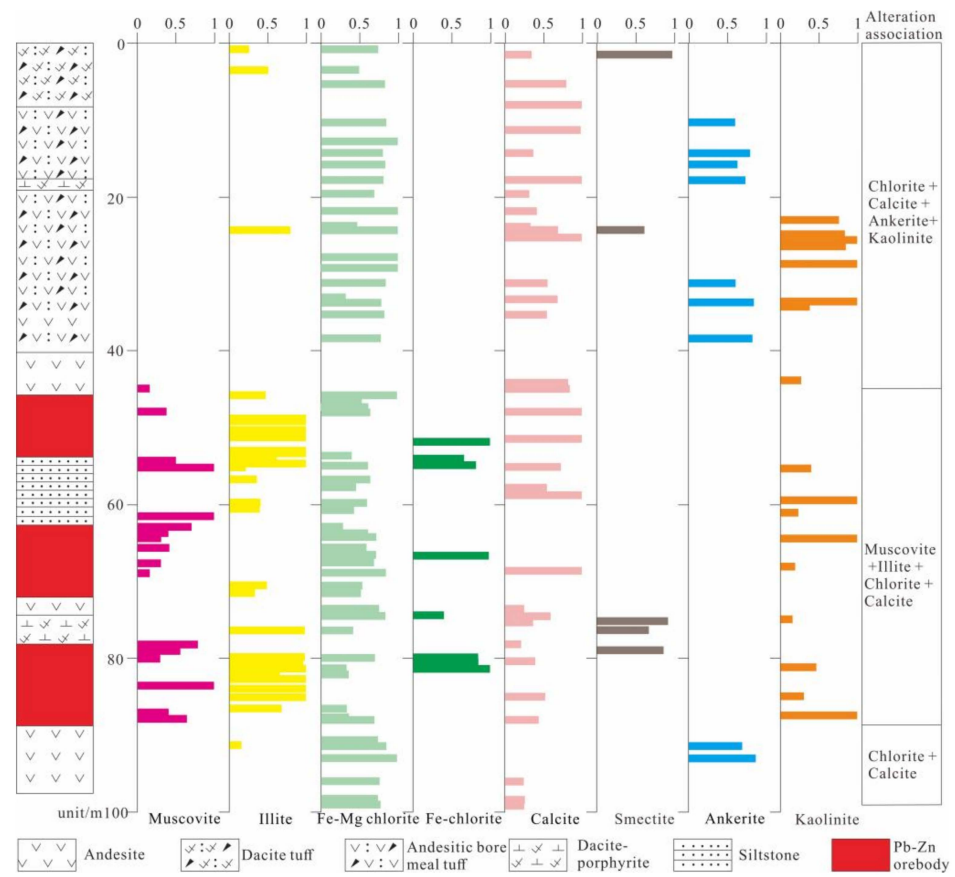


Figure 7. Alteration mineral zones in ZK20(0)1'02.

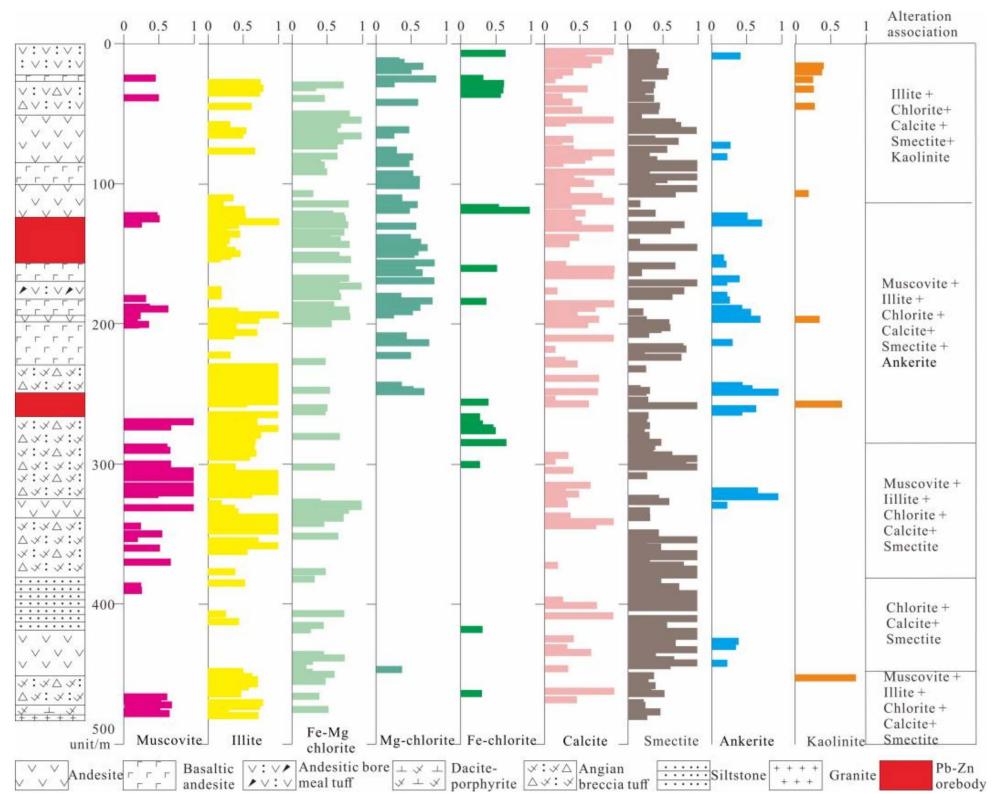


Figure 8. Alteration mineral zones in borehole ZK2115-1.

5. Discussion

5.1. Indicators of Hydrothermal Centers

The formation temperature of the minerals is directly correlated with the absorption peak wavelength of Fe–OH in chlorite minerals (pos2260) and the crystallinity index (CSM) [6–8,13–20]. CSM scalar values greater than 1 are indicative of chlorite with a high metamorphic grade, while values less than 1 are generally associated with chlorite produced by lower temperature alteration events; the higher the CSM value, the higher the alteration temperature [1–3,8–13]. The compositions of many minerals that contain Fe–OH have slightly changed. This indicates fluid chemicals are involved during the alteration. These compositional changes cause the wavelength position of the Fe–OH absorption feature to shift at around 2260 nm. It indicates the geochemical conditions during the alteration [6–8]. In most cases, the absorption trough for Fe-rich chlorite occurs between 2260 and 2265 nm, while the absorption peak for Mg-rich chlorite lies between 2255 and 2260 nm [11,22]. Fe-chlorite is cooled prior to Mg-chlorite, followed by Mg-Fe chlorite, Fe-Mg chlorite, and finally Mg-chlorite [3,5].

The formation temperature of the minerals is closely linked to the absorption peak wavelength of Al–OH in muscovite minerals (Pos2200) and the crystallinity index (ISM) [19,20]. ISM scalar values greater than 1 are indicative of illite with a high metamorphic grade, while values less than 1 are generally associated with illite produced by lower temperature alteration events; the higher the ISM value, the higher the alteration temperature [1–3,8–13]. The chemical composition of the fluids changed during alteration, leading to wavelength shifts in the absorption features. For adsorbed water, it was at approximately 1,900 nm, and for Al–OH, it was at around 2200 nm. As the alteration became stronger, the adsorbed water gradually diminished. Moreover, both the absorption peak wavelength of the Al–OH feature within the range of 2160 nm to 2240 nm and the crystallinity index increased [6–8,13–20]. Therefore, the wavelength position can indicate the geochemical conditions during the alteration.

This study mapped out the mineral alteration in the middle section (200 m) of the borehole drills and tunnels (Figure 9) and integrated the results with the compilation work. The illitization (of the muscovite group) Al–OH absorption peak wavelength within the 200 m middle section spreads across the area between the 1' and 17' lines, with a predominance at <2206 nm. This distribution shows a good correlation with the No. 2 ore body. The crystallinity of illite, with values > 1.1, forms a distinct belt extending from north to west, with two anomalous centers concentrated at the 1' and 5'–9' lines. In the case of chloritization (of the chlorite group), the Fe–OH absorption peak wavelength shows a sheet-like anomaly at >2254 nm along the 0'–7' lines. This continuous anomaly extends up to 500 m long and 20 m wide further northwest, which is similar to the direction of the ore body. This study has also located a northwestward weak anomaly (circumscribed by values > 2251) in the deeper section along the 15' line. There is an anomalous zone along the 9' and 17' lines with crystallinity of chlorite larger than 3.0. Additionally, combined with the engineering practice of the middle section at 0 m, chloritization (of the chlorite group) shows a sheet-like anomaly at the 1' line, with the Fe–OH absorption peak wavelength exceeding 2254 nm. This anomaly extends approximately 50 m long and 20 m wide to the northwest, which is similar to the direction of the ore body. It continues to stretch in the southeastern or southwestern direction.

According to the study, in the deep area of the Jiawula mine, the zones with deep possible hydrothermal activity are characterized by a lower wavelength (<2206 nm) of illitization (Al–OH absorption peak) and higher crystallinity index (>1.1), as well as a higher wavelength (>2254 nm) of chloritization (Fe–OH absorption peak) and higher crystallinity index (>3.0). Consistent with the pattern observed in the northeast-oriented profile, the Pos2200 values decrease from high values in the mineralization center to low values in the peripheral regions (Figure 9).

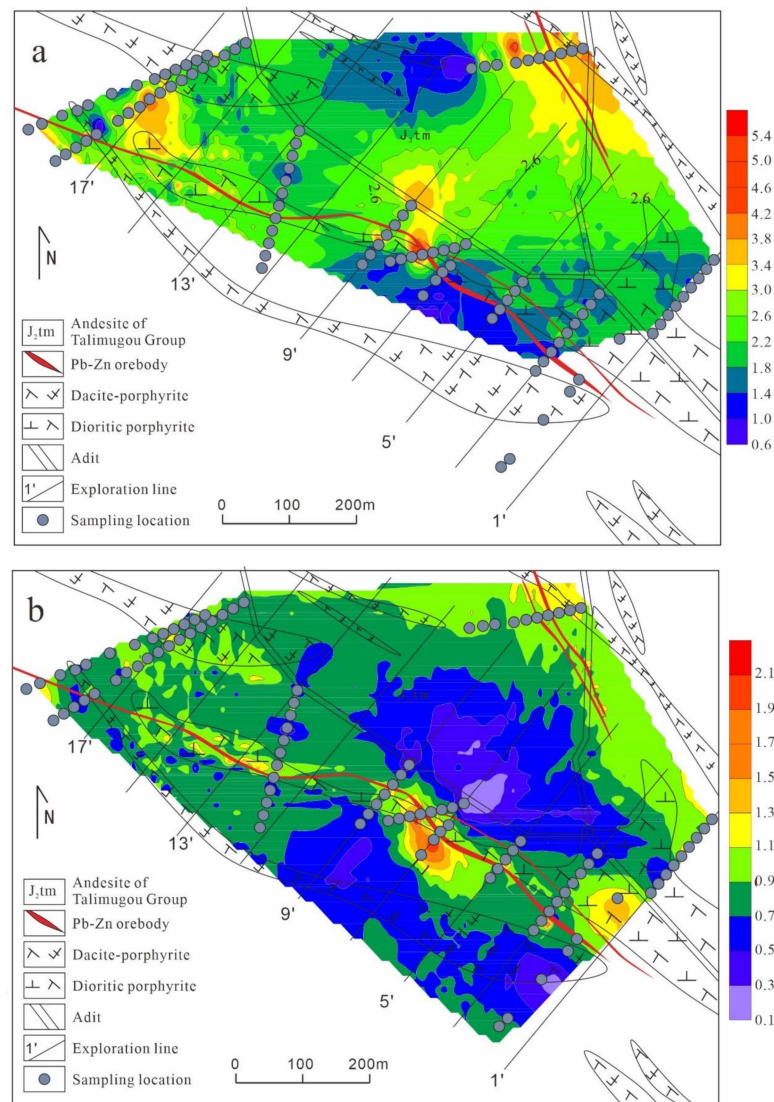


Figure 9. The contour lines of chlorite and illite crystallinity in the intermediate section (200 m) of the Jiawula deposit. (a) The contour lines of chlorite crystallinity. (b) The contour lines of illite crystallinity.

Based on the records about the boreholes and tunnels, this area mainly comprises fine grains and a network of galena-sphalerite veins and diabase rocks (Figure 10c). The groundmass is strongly silicified. This pattern was consistent with the comb-textured quartz + illite + Fe-chlorite + calcite alteration zones that had been delineated in tunnel records (Figure 10a), particularly the presence of Fe-chlorite (Figure 10b). The weakly altered zones were located near the eastern side of the area, suggesting another type of alteration. This assemblage was composed of comb-textured quartz + calcite + Fe-Mg chlorite + kaolinite, which was closer to the country rocks. Chloritization was also widespread in andesite and andesitic crystal tuffaceous breccia. However, based on mineral classification, such chloritization was primarily dominated by Fe-Mg chlorite, belonging to early wall-rock alteration. On the other hand, chloritization in the mineralized body and its surroundings was mainly characterized by Fe-chloritization, indicating that there was an elevation in temperature as a result of a certain geological process. Therefore, we can infer that there was a change in chlorite from Fe-Mg chlorite to Fe-chlorite. In the hydrothermal breccia near the mineralized body, the breccia consisted of andesite and andesitic tuffaceous breccia. According to our speculation, the diabase experienced two stages, with the first stage being early intrusion and the second stage being mineralization. The intrusion of the second-stage

diabase caused temperature changes near the mineralized body, in which Fe-chlorite was the dominant chlorite, with a maturity index > 3.0.

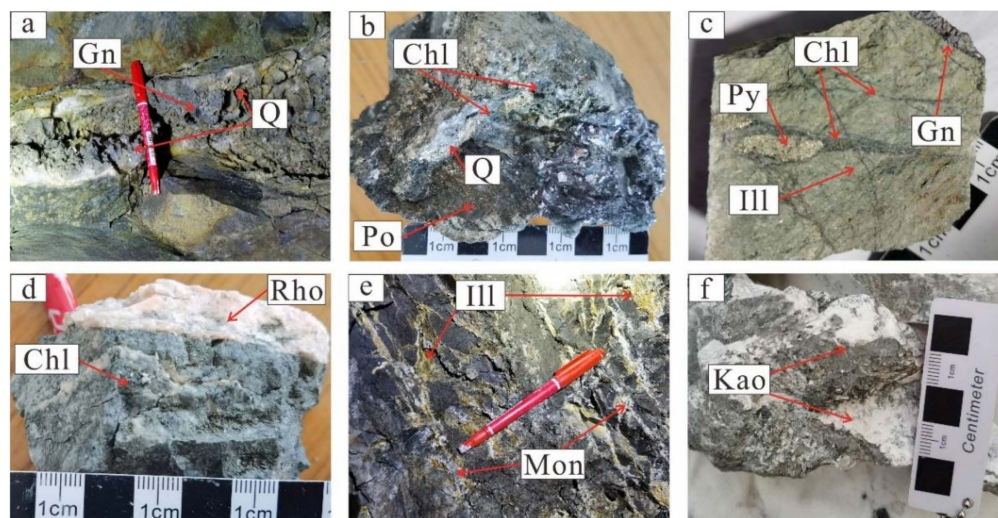


Figure 10. Photographs of major mineralization and alteration relationships in the Jiawula deposit: (a) smoke gray comb quartz, granular galena can be seen; (b) quartz vein filled with hydrothermal breccia, massive galena pyrrhotite cement, visible Fe-chlorite breccia; (c) yellow-green strong illite dacite porphyrite, late ferrochlorite network veins, fine-grained pyrite cluster spots can be seen along the chlorite edge; (d) rhodochroite and chlorite surrounding andesite; (e) illite and montmorillonite in the andesitic tuff in the outer zone of the ore body; (f) diffuse planar kaolinite in andesite. Q—quartz; Py—pyrite; Po—pyrrhotite; Gn—galena; Chl—chlorite; Ill—illite; Rho—rhombosite; Mon—montmorillonite; Kao—kaolinite.

5.2. Exploration Significance

According to the results of SWIR spectroscopy, the mineralized area in this study mainly involved illitization and chloritization. They are widely distributed in andesite, andesitic crystal tuffaceous breccia, gabbroic diorite, and diabase of the study area.

In borehole ZK2115-1, Pos2200 exhibited a steady change, in which the Al–OH absorption peak at 122.5–128.35 m had a slight tendency to decrease. At the depth ranges of 122.5–128.35 m, 200 m, and 300–350 m, the illite’s crystallinity index was greater than 1.0, while the chlorite’s crystallinity index was greater than 3.0 when the depth ranges were 122.5–200 m and 350 m (Figure 11, left). At the 122.5–128.35 m deep mineralized zone, the primary rock was andesite. In the fractures, we found yellowish calcite–quartz veins. Along the calcite veins, we observed scattered occurrences of pyrite and sphalerite in spots, blocks, and sparsely disseminated forms. There was a strong chloritization, so the rock was fragmented. A number of calcite–quartz veins developed at 127–127.75 m, indicating a good mineralization. At 247.20–248.40 m, the lead–zinc mineralization was present, with speckled pyrite, galena, and sphalerite occurring along the calcite–quartz veins in fractures. At 257–257.7 m, the rock was loosely cemented and was made up of chloritized and illitized manganese rhodochrosite (Figure 10d), along with a network of fine-grained quartz–calcite veins.

In the ZK20(0)1’02 section, muscovitic illite most probably occurred within 48.9 to 54.8 m and 80 to 86.6 m from the surface (Figure 7). At the interval of 48.9 to 54.8 m, the dominant minerals included Fe-chlorite, illite, and calcite. The 80–86.6 m interval comprised Fe-Mg chlorite, illite, and smectite (Figure 10e). The strongest mineralization occurred at the depth of 48.9 to 54.8 m, with a remarkable Pb of 29.35%, Zn of 12.14%, Ag of 301 g/t, and Cu of 0.2%.

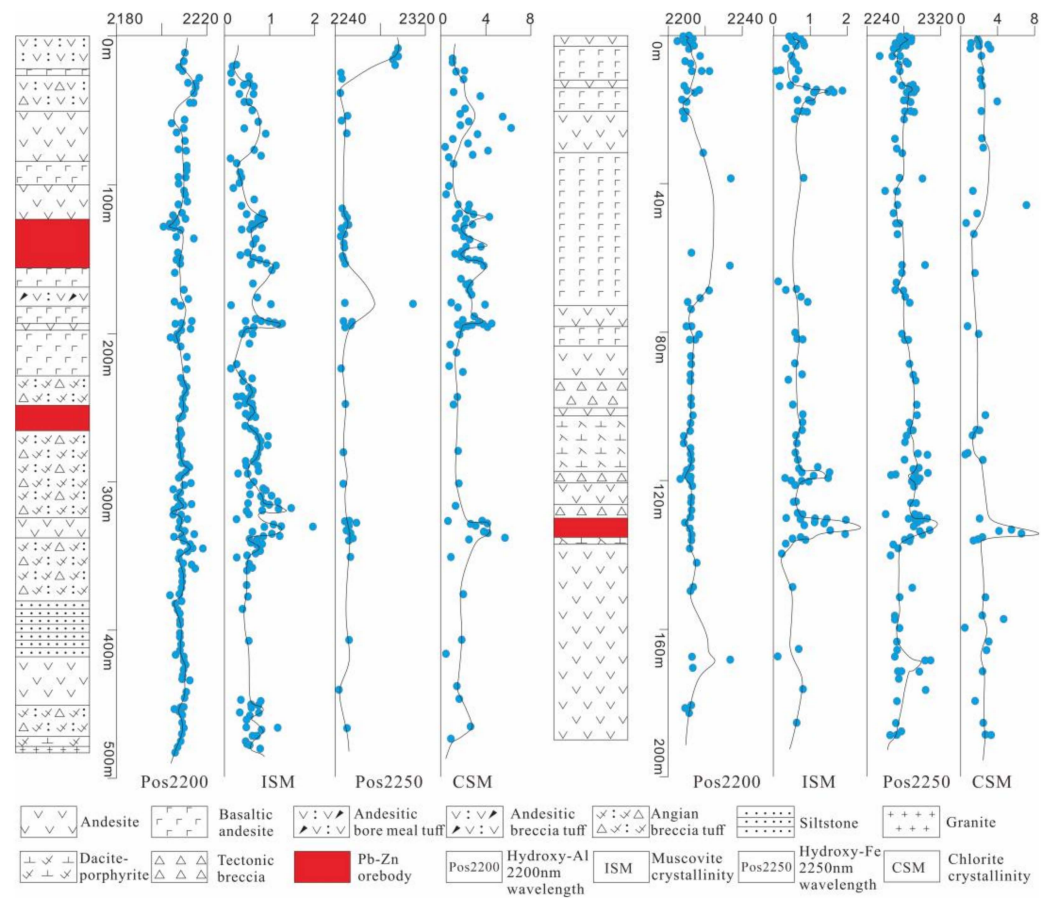


Figure 11. Variations in characteristic parameters of muscovite and chlorite in ZK2115-1 (left) and ZK13'03 (right).

In borehole ZK13'03, Pos2200 exhibited a steady variation. However, at the depth of 120.6–137.25 m, the illite crystallinity, Pos2350, and chlorite crystallinity increased significantly (Figure 11, right). The interval from 130.15 to 135.27 m was mineralized. Its rock type was andesite, with strong chloritization, illitization, and kaolinization (Figure 10f). Fine veins of lead galena, sphalerite, and pyrite developed along the fractures. At 130.15–130.50 m, there was the development of quartz veins and abundant pyrite, lead galena, and sphalerite occurring along the fractures. They occurred in blocks and densely disseminated forms, The lead–zinc–iron mineral veins were later intersected and cut by quartz veins. From 133.18 to 134.58 m, lead galena, sphalerite, and pyrite developed along the fractures in veins or disseminated forms.

According to our comprehensive analysis, the lead–zinc mineralization is closely linked to the later-stage fracturing alteration in the diabase and andesite and a high illite crystallinity index (>1.1) [6–8]. The content of Pb–Zn–Ag is generally higher when the Fe–OH absorption peak wavelength of chlorite (>2254) and the crystallinity index (>3.0) are larger [13–20]. Moreover, the dominant chlorite is Fe-chlorite. Therefore, the lithological alteration and high-grade mineralization correspond reasonably well with the diabase + andesite–Fe-chlorite + illite. In subsequent exploration, we need to focus on fractured and chloritized diabase distributed in deep areas because these geological characteristics are often linked to the mineralization.

6. Conclusions

- (1) By measuring the deep and surface altered rocks in the Jiawula lead–zinc deposit with SWIR spectroscopy, this study identified a total of 16 hydroxyl-bearing altered minerals. The minerals included chlorite (Fe–Mg chlorite, Mg-chlorite, and Fe-chlorite),

sericite (muscovite, paragonite, phengite), illite (muscovite illite, paragonite illite, phengite illite), calcite, ankerite, kaolinite, and smectite. Based on the geological characteristics and TSG spectroscopic interpretation results, we established horizontal and vertical alteration zones for the deposit. The zones consisted of comb-textured quartz–illite–Fe–chlorite–carbonate veins → muscovite–illite–chlorite–ankerite veins → illite–smectite–chlorite veins → chlorite–kaolinite–calcite veins.

In borehole ZK19 (200) 13'03, Mg–chlorite was mainly distributed at the upper part of the borehole, while Fe–chlorite was mainly concentrated in the lower part. In borehole ZK20(0)1'02, no Mg–chlorite was found, and Fe–chlorite was mainly distributed in the lower part. Sericite illite was surrounded by ankerite on both sides. In borehole ZK2115-1, Mg–chlorite alteration occurred mainly in the upper part, and Fe–chlorite was concentrated in the three blocks in the upper part of the borehole.

- (2) The crystallinity of illite, with values > 1.1, forms a distinct belt extending from north to west, with two anomalous centers concentrated at the 1' and 5'–9' lines. The crystallinity of chlorite, with values > 3.0, shows two anomalous centers concentrated at the 9' and 17' lines. So, the hydrothermal centers of the Jiawula mine are probably located in the deep areas where the Al–OH absorption peak wavelength of illitization (<2206 nm) is small with a high crystallinity index (>1.1) and where the Fe–OH absorption peak wavelength of chloritization (>2254 nm) is high with an even higher crystallinity index (>3.0).
- (3) By delineating the hydrothermal centers and showing their spatial relationship with the known ore bodies, we established a lithological alteration–high-grade mineralization correlation with the diabase + andesite–Fe–chlorite + illite. In future exploration, we recommend paying attention to the distribution of deeply fractured chloritized diabase because these geological characteristics are often linked to mineralization.

Author Contributions: Conceptualization, L.W., W.F. and Z.Y.; methodology, L.W. and G.G.; software, L.W., Z.L. and G.G.; validation, L.W.; formal analysis, L.W. and D.W.; investigation, L.W., Z.L. and G.G.; writing—original draft preparation, L.W., Z.Y. and W.F.; writing—review and editing, L.W. and Z.Y.; visualization, L.W. and Z.Y.; supervision, L.W. project administration, L.W. All authors have read and agreed to the published version of the manuscript.

Funding: This work was financially supported by the Technology Plan Project of Yunnan Chihong Zn & Ge Co., Ltd. (Grant No. 202106CHRDKCB02).

Institutional Review Board Statement: Not applicable.

Informed Consent Statement: Not applicable.

Data Availability Statement: The raw data supporting the conclusions of this article will be made available by the authors on request.

Acknowledgments: The authors thank the team members at CUGB for their field support, data analysis, constructive discussions, and comments.

Conflicts of Interest: The authors declare that this study received funding from Yunnan Chihong Zn & Ge Co., Ltd. The funder was not involved in the study design, collection, analysis, interpretation of data, the writing of this article or the decision to submit it for publication.

References

1. Clark, R.N. Spectroscopy of rocks and minerals, and principles of spectroscopy. *Remote Sens. Earth Sci. Man. Remote Sens.* **1999**, *3*, 3–58.
2. Hecker, C.; van Ruitenbeek, F.J.A.; van der Werff, H.M.A.; Bakker, W.H.; Hewson, R.D.; van der Meer, F.D. Spectral Absorption Feature Analysis for Finding Ore: A Tutorial on Using the Method in Geological Remote Sensing. *IEEE Geosci. Remote Sens. Mag.* **2019**, *7*, 51–71. [[CrossRef](#)]
3. Van der Meer, F.; Kopačková, V.; Koucká, L.; van der Werff, H.M.A.; van Ruitenbeek, F.J.A.; Bakker, W.H. Wavelength feature mapping as a proxy to mineral chemistry for investigating geologic systems: An example from the Rodalquilar epithermal system. *Int. J. Appl. Earth Obs. Geoinf.* **2018**, *64*, 237–248. [[CrossRef](#)]

4. Simpson, M.P. Reflectance spectrometry [SWIR] of alteration minerals surrounding the Favona epithermal vein. Waihi vein system, Hauraki Goldfield. In Proceedings of the AusIMM New Zealand Branch Annual Conference, Reefton, New Zealand, 30 August–2 September 2015.
5. Thompson, J.B.; Hauff Phoebe, L. Alteration mapping in exploration; application of short-wave infrared SWIR spectroscopy. *SEG Newsl.* **1999**, *30*, 1–27. [[CrossRef](#)]
6. Dill, H.G. PIMA—Supported exploration of industrial minerals in Mongolia and Thailand. *Erzmetall* **2003**, *56*, 20–28.
7. Calvin, W.M.; Pace, E.L. Mapping alteration in geothermal drill core using a field portable spectroradiometer. *Geothermics* **2016**, *61*, 12–23. [[CrossRef](#)]
8. Wang, C.W.; Guo, N.; Guo, K.; Zhang, T.T.; Chong-Wu, W.; Na, G.; Ke, G.; Ting-Ting, Z. Characteristics of the chlorite alteration in the porphyry-skarn deposit based on short-wave infrared technology: A case study of the jiama copper-polymetallic deposit in Tibet. *Geol. Explor.* **2014**, *50*, 1137–1146.
9. Yang, K.; Lian, C.; Huntington, J.F.; Peng, Q.; Wang, Q. Infrared Spectral Reflectance Characterization of the Hydrothermal Alteration at the Tuwu Cu-Au Deposit, Xinjiang, China. *Miner. Depos.* **2005**, *40*, 324–336. [[CrossRef](#)]
10. Chang, Z.S.; Yang, Z.M. Evaluation of Inter-instrument Variations Among Short Wavelength Infrared (SWIR) Devices. *Econ. Geol.* **2012**, *107*, 1479–1488. [[CrossRef](#)]
11. Xiu, L.C.; Zheng, Z.Z.; Yu, Z.K.; Huang, J.J.; Yin, L.; Wang, M.J.; Zhang, Q.N.; Huang, B.; Chen, C.X.; Xiu, T.J.; et al. Mineral Analysis Technology Application with Near Infrared Spectroscopy in Identifying Alteration Mineral. *Acta Geol. Sin.* **2007**, *81*, 1584–1590.
12. Xu, Q.S.; Qin, F.; Liu, Y.; Yuan, B.; Sun, H.; Chen, X.F.; Zheng, J.; Niu, X.L. Lithocaps: Geological characteristics and implication to exploration of epithermal and porphyry-style deposits. *Geol. Explor.* **2010**, *46*, 20–23.
13. Yang, Z.M.; Hou, Z.Q.; Yang, Z.S.; Qu, H.C.; Li, Z.Q.; Liu, Y.F. Application of short wavelength infrared (SWIR) technique in exploration of poorly eroded porphyry Cu district: A case study of Niancun ore district, Tibet. *Miner. Depos.* **2012**, *31*, 699–717.
14. Xu, C.; Chen, H.Y.; White, N.; Qi, J.P.; Zhang, L.J.; Zhang, S.; Duan, G. Alteration and mineralization of Xinan Cu-Mo ore deposit in Zijinshan orefield, Fujian Province, and application of short wavelength infra-red technology (SWIR) to exploration. *Miner. Depos.* **2017**, *36*, 1013–1038.
15. Zhang, S.T.; Chen, H.Y.; Zhang, X.B.; Zhang, W.F.; Xu, C.; Han, J.S.; Chen, M. Application of short wavelength infrared (SWIR) technique to exploration of skarn deposit: A case study of Tonglvshan Cu-Fe-Au deposit, Edongnan (southeast Hubei) ore concentration area. *Miner. Depos.* **2017**, *36*, 1263–1288.
16. Huang, Y.R.; Guo, N.; Zheng, L.; Yang, Z.Y.; Fu, Y. 3D Geological Alteration Mapping Based on Remote Sensing and Shortwave Infrared Technology: A Case Study of the Sinongduo Low-sulfidation Epithermal Deposit. *Acta Geosci. Sin.* **2017**, *38*, 779–789.
17. Wang, J.R.; Lv, X.B.; Huang, Z.Q.; Sun, H.; Qin, Z.P.; Zou, R.X.; Fan, X.L.; Huang, X.Y. A study of near—Infrared spectroscopy on altered minerals in the Nuri copper—Polymetallic deposit, Tibet. *Geol. Explor.* **2017**, *53*, 141–150.
18. Chen, S.B.; Huang, B.Q.; Li, C.; Tian, Q.L.; Wang, C.; Wu, J.X.; Chen, M.X.; Han, J.S.; Feng, Y.Z.; Wang, Y.F. Alteration and Mineralization of the Yuhai Cu Deposit in Eastern Tianshan, Xinjiang and Applications of Short Wave length Infra-Red (SWIR) in Exploration. *Earth Sci.* **2018**, *43*, 2911–2928.
19. Ren, H.; Zheng, Y.Y.; Wu, S.; Zhang, X.; Ye, J.W.; Chen, X.D. Short-Wavelength Infrared Characteristics and Indications of Exploration of the Demingding Copper-Molybdenum Deposit in Tibet. *Earth Sci.* **2020**, *45*, 930–944.
20. Tang, N.; Lin, B.; Li, Y.B.; Wang, Y.Y.; Li, J.J. Application of short-wave length infrared spectroscopy in porphyry-epithermal system: A case study of Tiegelongnan super-large copper(gold)deposit, Tibet. *Acta Geol. Sin.* **2021**, *95*, 2613–2627.
21. Liu, B.H.; Liu, H. Short-wave infrared spectroscopy study on wall rock alteration of the Gan-zhuershande silver-lead-zinc deposit in Inner Mongolia. *Geol. Explor.* **2016**, *52*, 703–711.
22. Liu, X.X.; Zhang, H.; Zhang, J.; Shi, W.X.; Zhang, X.L.; Cheng, J.W.; Lu, K.X. A Study on Alteration Mineral Assemblages and Mineralization Characteristics of a Wunugetushan Porphyry Copper-Molybdenum Deposit in Inner Mongolia, China, Based on Infrared Spectroscopy. *Rock Miner. Anal.* **2021**, *40*, 121–133.
23. Tian, F.; Leng, C.b.; Zhang, X.c.; Tian, Z.d.; Zhang, W.; Guo, J.h. Application of Short Wavelength Infrared Technique in Exploration of Mineral Deposits: A Review. *Bull. Mineral. Petrol. Geochem.* **2019**, *38*, 634–642.
24. Pan, L.j.; Sun, E.S. Geological Characteristics of the Jiawula Silver-Lead-Zinc Deposit, Inner MONGOLIA. *Miner. Depos.* **1992**, *11*, 45–53.
25. Zhao, Y.M.; Zhang, Q. *Metallogenic Regularity and Prospect Evaluation of Copper-Polymetallic Deposits in Greater Khingan and Its Adjacent Areas*; Seismological Press: Beijing, China, 1997; pp. 20–60.
26. Nie, F.J.; Liu, Y.; Liu, Y.F.; Jiang, S.H.; Zhang, K.; Liu, Y. Ore-Forming Processes of Silver-Polymetallic Deposits Occurring Within Tsav-Jiawula Region Along China-Mongolian Border. *J. Jilin Univ. (Earth Sci. Ed.)* **2011**, *41*, 1715–1725.
27. Jiang, S.H.; Nie, F.J.; Zhang, Y.; Hu, P. The Latest Advances in the Research of Epithermal Deposits. *Earth Sci. Front.* **2004**, *11*, 401–411.
28. Zhai, D.G.; Liu, J.J.; Wang, J.P.; Yao, M.J.; Liu, X.W.; Liu, Z.J.; Wu, S.H.; Fu, C.; Wang, S.G.; Li, Y.X. A study of stable isotope geochemistry of the Jiawula large Pb-Zn-Ag ore deposit, Inner Mongolia. *Earth Sci. Front.* **2013**, *20*, 213–225.
29. Liu, G.X.; Zhang, C.P.; Lv, J.C.; Zhang, P. Zircon U-Pb Chronology of Quartz Monzoporphyry In Jiawula Pb-Zn-Ag Deposit, Daxinganling Mountains: Geological Implications. *Geol. Resour.* **2018**, *27*, 424–430.

30. Meng, Z.J.; Qin, K.Z. Geological Characteristics, Ore-Forming Center and Prognosis for Concealed Orebodies of The Jiawula-Chagan Polymetallic Ore Field in Inner Mongolia. *Geol. Explor. Non-Ferr. Met.* **1997**, *6*, 25–31.
31. Yang, M.; Sun, J.G.; Wang, Z.Y.; Zhao, S.F.; Liu, C.; Feng, Y.Y.; Ren, Z.N. Petrogenesis and Geological Significance of the Alkali-Rich Granite Porphyry in the Jiawula Cu-Ag-Pb-Zn Deposit in the Western Slope of the Great Xing'an Range: Zircon U-Pb Dating and Geochemical Characteristics. *J. Jilin Univ. (Earth Sci. Ed.)* **2017**, *47*, 477–496.
32. Niu, S.S.; Li, S.R.; Guo, J.; Zhao, W.B. Elemental Distribution and Mineral Potential of the No.2 Ore Body in the Jiawula Pb-Zn-Ag Deposit, Inner Mongolia, China. *Bull. Mineral. Petrol. Geochem.* **2019**, *38*, 759–765.
33. Gao, Y.; Liu, J.; Li, T.G.; Zhang, D.D.; Yang, Y.C.; Han, S.J.; Ding, Q.F.; Zhang, S. Multiple isotope (He-Ar-Zn-Sr-Nd-Pb) constraints on the genesis of the Jiawula Pb-Zn-Ag deposit, NE China. *Ore Geol. Rev.* **2021**, *134*, 104142. [[CrossRef](#)]
34. Liu, J.; He, J.C.; Lai, C.K.; Wang, X.T.; Li, T.G. Time and Hf isotopic mapping of Mesozoic igneous rocks in the Argun massif, NE China: Implication for crustal architecture and its control on polymetallic mineralization. *Ore Geol. Rev.* **2022**, *141*, 104648. [[CrossRef](#)]
35. Li, T.G.; Wu, G.; Liu, J.; Wang, G.R.; Hu, Y.Q.; Zhang, Y.F.; Luo, D.F.; Mao, Z.H.; Xu, B. Geochronology, fluid inclusions and isotopic characteristics of the Chaganbulagen Pb–Zn–Ag deposit, Inner Mongolia, China. *Lithos* **2016**, *261*, 340–355. [[CrossRef](#)]
36. Niu, S.D.; Li, S.R.; Jan, M.H.; Santosh, M.; Zhang, D.H.; Zeng, Y.J.; Li, Z.D.; Zhao, W.B. Zircon U-Pb geochronology and geochemistry of the intrusions associated with the Jiawula Ag-Pb-Zn deposit in the Great Xing'an Range, NE China and their implications for mineralization. *Ore Geol. Rev.* **2017**, *86*, 35–54. [[CrossRef](#)]
37. Niu, S.D.; Li, S.R.; Jan, M.H.; Santosh, M.; Zhang, D.H.; Zeng, Y.J.; Li, Z.D. $^{40}\text{Ar}/^{39}\text{Ar}$ geochronology, fluid inclusions, and ore-grade distribution of the Jiawula Ag–Pb–Zn deposit, NE China: Implications for deposit genesis and exploration. *Geol. J.* **2020**, *55*, 1115–1127. [[CrossRef](#)]
38. Dai, M.; Yan, G.S.; Liu, C.; Deng, J.F.; Li, Y.S.; Jia, W.B.; Lai, C.K. Southward subduction of the Mongolia–Okhotsk Ocean: Insights from Early–Middle Triassic intrusive rocks from the Jiawula–Tsagenbulagen area in NE China. *Geol. J.* **2020**, *55*, 967–993. [[CrossRef](#)]
39. Cao, P.; Ren, Y.S.; Hou, Z.S.; Wang, X. Ore-forming fluid characteristics and mineralization age of the Jiawula Pb–Zn(Ag) Deposit in Manzhouli area. *Gold* **2018**, *39*, 5–12.

Disclaimer/Publisher's Note: The statements, opinions and data contained in all publications are solely those of the individual author(s) and contributor(s) and not of MDPI and/or the editor(s). MDPI and/or the editor(s) disclaim responsibility for any injury to people or property resulting from any ideas, methods, instructions or products referred to in the content.